First-principles investigation of silicon-substituted hybrid halide perovskites for lead-free optoelectronic applications

I.Salym[a,b],R. Takassa[a], O. Farkad[a], F. Elfatouaki[a], A. El Mouncharih[a], M. El Aatmani[b], D. Abouelaoualim[a], and A. El Boujlaidi[a]

[a]*LaMEE, Department of Physics, Faculty of Sciences Semlalia, Cadi Ayyad University, Marrakech, Morocco,*
[b]*Laboratory of Materials Science and Process Optimization, Faculty of Sciences Semlalia, Cadi Ayyad University, Marrakech, Morocco*
e-mail: i.salym.ced@uca.ac.ma

Received 21 April 2025; accepted 13 April 2026

Organic–inorganic halide hybrid perovskites have been extensively investigated for a range of optoelectronic applications, including tandem solar cells. However, instability and lead toxicity in widely studied hybrid halide perovskites (HHPs) necessitate the exploration of non-toxic semiconductor alternatives.

Here, we investigate the structural and optoelectronic properties of formamidinium silicon iodide ($FASiI_3$) using two complementary computational frameworks: the GGA-PBE functional and TB-mBJ exchange-correlation potential. Our results show that $FASiI_3$ crystallizes in a cubic lattice (space group Pm|3m) with an equilibrium lattice parameter $a = 6.29$ Å.

Electronic structure calculations reveal that the TB-mBJ approach provides a more reliable description of $FASiI_3$ semiconducting behavior, yielding a direct band gap conducive to photovoltaic operation. Optical analyses indicate pronounced anisotropy in the reflectivity and absorption spectra along the (xx) and (zz) axes, with absorption coefficients exceeding 10^5 cm^{-1} in the near-infrared (NIR) region of the solar spectrum. These findings underscore $FASiI_3$ potential as a lead-free, environmentally benign perovskite with robust light-harvesting capabilities for next-generation photovoltaic and optoelectronic devices.

Keywords: Formamidinium Halide perovskite; silicon compounds; DFT; optoelectronic properties.

DOI: https://doi.org/10.31349/RevMexFis.72.041005

1. Introduction

Organic-inorganic hybrid halide perovskites (HHP) have recently been used in a variety of optoelectronic applications, including tandem solar cells [1], scintillator [2], and medical imaging [3].

The best-known, such as MAPI and FAPI, have shown great potential, but their poor stability under environmental conditions, such as humidity, oxygen, UV exposure, and high temperatures, limits their durability [4,5]. In addition, the use of lead in these materials poses a serious toxicity problem, contributing to electronic pollution from e-waste [6]. The development of new, more stable, and environmentally friendly lead-free perovskites has thus become a major challenge for the improvement of optoelectronic devices. Silicon is a promising solution to these problems. It offers hybrid perovskites better stability thanks to their resistance to environmental factors, while reducing their toxicity [7]. What's more, it helps limit the ecological impact of optoelectronic devices by reducing pollution linked to e-waste. Its abundance and ease of extraction make it a key material for various industrial applications, including electronics, optoelectronics, and solar energy.

In fact, HHP materials possess very important optoelectronic properties, such as a high absorption coefficient, high mobility of charge carriers, and a direct band gap [8]. ABX_3 is the chemical formula of HHP [9], in which the organic molecule (CH_3NH_3 (MA), $CH(NH_2)_2$ (FA), EA...) is a monovalent cation occupying the A-site, the divalent cation (Ge^{2+}, Sn^{2+}, Si^{2+} ...) occupies the B-site, while the X-site is occupied by a halogen anion (Cl^-, Br^-, I^-), or by a percentage of each element between them. The quality of these HHP materials is determined by the stable moment of a cation of an organic molecule that exists at the A-site [10].

Lead-based formamidinium halide perovskites, $FAPbX_3$, were reported to have the smallest band gap, which was equal to 1.48 eV [11] and 1.30 eV in Ref. [12]. S. Pachori *et al.* have investigated the fundamental properties of $FAPbI_3$ using DFT calculations coupled with PBEsol and WC-GGA exchange-correlation potentials. Their theoretical analysis reveals a direct band gap of around 1.30 eV at the R point and an absorption coefficient in excess of 10^4 cm^{-1} in the visible spectrum [8]. F. Mahajabin *et al.* explored the effect of compressive and tensile stresses on the optoelectronic and dielectric properties of the cubic perovskite $FAPbI_3$ using DFT calculations, with and without spin-orbit coupling (SOC). The results show that the band gap of 1.74 eV for the unstressed material decreases under compressive stress and increases under tensile stress, except at +6% stress, where it decreases. With SOC, the band gap becomes indirect, dropping to 0.66 eV. Compressive stress improves the static dielectric constant, while tensile stress reduces it. Optical properties reveal a blue shift with compression and a red shift with tension, as well as increased absorption in the visible and UV regions [13]. But because of the toxicity of lead, researchers are exploring new ways to replace it with other non-toxic ma-

terials [14], choosing other inorganic cations for their high stability. For example, P. Kanhere studied the effect of Sn doping on the physical properties of lead-based methylammonium iodide perovskites using DFT and found that this doping altered the electronic band structure [15]. To improve stability, they also proved that changing the X halogens (I, Br, and Cl) had an effect on the band gap, and found that when they made a mixture of halogens, stability improved, as did efficiency [16]. In this study, based on the similarity between the Pb^{2+} ion and the Si^{2+} ion in terms of electronic configuration and van der Waals radius (r(Pb^{2+}) = 220 pm and r(Si^{2+}) = 210 pm) [17], we proposed replacing lead with silicon and investigating the compound $FASiI_3$. To this end, we used the DFT method with GGA-PBE and TB-mBJ exchange-correlation potentials to explore the effect of silicon on the optoelectronic properties of hybrid perovskites with a view to their use in various applications. We used GGA-PBE for structural property optimization because of its ability to accurately predict material geometrical parameters while offering a good compromise between accuracy and computational cost [18]. For electronic and optical properties, GGA-PBE is used for an initial estimate of electronic properties, while TB-mBJ is applied to improve the accuracy of the band gap and optical spectra, offering a more realistic description of the material's electronic and optical behavior [16,19]. This paper, in Sec. 2, provides a brief explanation of the computational method used. In Sec. 3, the theoretical calculations of structural and optoelectronic properties are presented and discussed. Finally, the results are summarized in the conclusion.

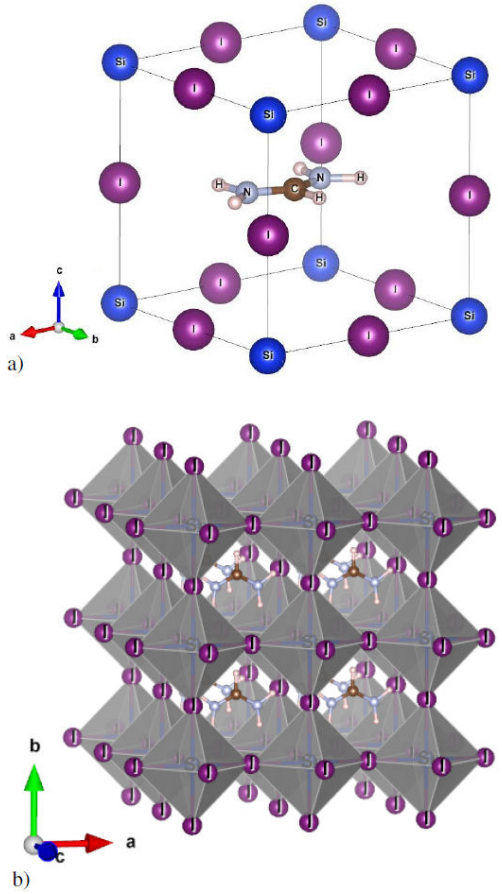

FIGURE 1. The structure of $FASiI_3$ a) side- view b) top-view.

2. Computational method

This study focuses on the theoretical analysis of the optoelectronic properties of $FASiI_3$. To this end, the `wien2k` software package, based on the full-potential linearized augmented plane wave (FP-LAPW) method, was used [20,21]. is employed for our computational work. In the FP-LAPW method, the potential and charge density inside the muffin-tin spheres are extended by spherical harmonics, while in the interstitial region, a basic set of plane waves is used [22]. For structural optimization, the GGA-PBE exchange-correlation function is used [23]. Calculations are performed with an expansion of the basis function of $R_{mt} \cdot K_{\max} = 3$ and a mesh of k-points = 1000 in the Brillouin zone to ensure high accuracy. Muffin-tin radii of 2.45, 2.40, 1.2, 1.3, and 0.65 a.u. are adopted for silicon, iodine, carbon, nitrogen, and hydrogen atoms, respectively, to reduce leakage and enable rapid energy convergence. The wave function is extended to lmax = 10 inside the atomic spheres, and the Gmax value of 20 Rydberg is used for the charge density's Fourier expansion. Self-consistency has been achieved when we obtain a total energy variation of less than 10^{-4} Ry per unit formula in successive iterations. The GGA-PBE and TB-mBJ approximations [24,25] were included in the calculation of electronic and optical properties [26], enabling in-depth study of the properties of $FASiI_3$

3. Results and discussion

3.1. structural properties

The geometry optimization of $FASiI_3$ compound studied here shows that this compound crystallizes in a cubic-oriented cell and its space group is Pm3m (no. 221) [27]. The cubic unit cell of halide perovskite has twelve atoms, as shown in Fig. 1. In this cubic structure, the Si^{2+} cation is in octahedral coordination with six iodine atoms SiI^6 octahedron. The interstitial site between the SiI^6 octahedra is occupied by the FA^+ cation.

The calculation of any physical properties can only be initiated if the structure is at a state of stability. In this regard, as shown in Fig. 2, the equilibrium volume of the cubic unit cell was determined by minimizing the total energy as a function of volume using Murnaghan's equation of state [28,29]:

$$E(V)=E_0+\frac{B_0V}{B_0'(B_0'-1)}\left[\left(\frac{V}{V_0}\right)^{1-B_0'}+(B_0'-1)\right]. \quad (1)$$

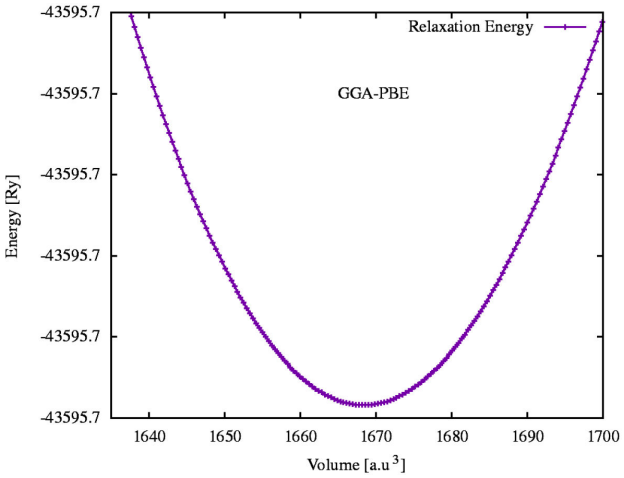

FIGURE 2. The total energy as a function of unit cell volume for $FASiI_3$.

TABLE I. Structural properties of the investigated compound.

Property	GGA-PBE	Other works
Lattice parameter (Å)	6.29	6.3 [27], 6.34 [30]
Bulk modulus (GPa)	48.31	–
Pressure derivative B'	4.42	–

Table I shows the equilibrium lattice parameter a, the bulk modulus B, and its pressure derivative (B').

The reaction of $FASiI_3$ can be described as:

$$FAI + SiI_2 \rightarrow FASiI_3. \quad (2)$$

To investigate the stability of $FASiI_3$, the formation energy per atom is computed through the the total energy calculation using the following formula [31]:

$$E_f(FASiI_3) = \frac{E(FASiI_3) - (E_C + 2E_N + 5E_H + E_{Si} + 3E_I)}{12}, \quad (3)$$

where $E(FASiI_3), E_C, E_N, E_H, E_{Si}$, and E_I are the total energys of $FASiI_3$, C, N, H, Si and I respectively wich are calculated taking into account the most stable structure of the elements.

$$E_f(FASiI_3) = -2.38\,\text{eV/atom}$$

The negative formation energy indicates that the material is thermodynamically stable [31], suggesting its potential feasibility for practical applications.

3.2. Electronic properties

HHPs are one class of materials with huge potential in tandem solar cell applications [32], due to some peculiar electronic properties that directly impact their ability to absorb light [33]. The major electronic properties include the band gap, the nature of the band structure, and DOS, all of which may be readily tuned by structural changes to the perovskite. This inherent flexibility, combined with their durability, makes silicon-based HHP a material of choice in the pursuit of highly efficient tandem solar cell devices [34]. An ideal band gap is fundamental in assessing the efficiency of a material in sunlight absorption. In the case of perovskites, an ideal band gap allows for efficient energy conversion, for it determines the number of photons coming from sunlight that may be absorbed and converted into electrical energy [35]. The band structure-being either direct or indirect also plays a major role in determining how efficient photon absorption and charge transport would be [36,37]. A direct band gap, the case of $FASiI_3$ studied here, can be particularly useful for tandem solar cell applications. Another important factor is DOS, *i.e.*, the density of states, which describes the number of electronic states at each energy level. By analyzing the DOS and contributions from different atomic orbitals, one can understand how electrons and holes would behave in this material [38] and, in consequence, the efficiency at which the photovoltaic device operates. In this work, to calculate electronic properties like band structure and DOS, two different exchange-correlation potentials have been used: GGA-PBE and TB-mBJ, within an energy range of [-5.0,5.0] eV about the Fermi level. From Fig. 3, it can be seen that the band structure presents a direct band gap at the symmetry R point. Band gap values calculated, compared to other previous calculations, are presented in Table II. The total density of states and partial density of states (TDOS, PDOS) respectively of C,N,H,Si and I, are presented in Figs. 4 and 5 respectively, with the Fermi energy level taken as zero energy reference.

TDOS plots and PDOS reveals a low density of states around the Fermi energy (0 eV), indicating semiconducting behavior for the $FASiI_3$ material [39], characterized by the presence of a band gap between the valence and conduction bands. In the valence band, a sharp peak is observed around -1 eV, mainly attributed to the p-orbitals of iodine atoms, with secondary contributions from the p-orbitals of silicon and nitrogen. Another significant peak appears in the region between 3 eV and 4 eV, with notable contributions from the p-orbitals of carbon, iodine and silicon atoms.

Comparing the different functionalities used, It is apparent that the use of the TB-mBJ functional significantly affects the DOS and PDOS. The TB-mBJ functional enhances and refines the peak intensities, thus allowing a more detailed characterization of electronic interactions [40]. Further, the conduction band also appears to be more dynamic in carbon atoms, insinuating that this functional describes better the manner in which carbon atoms modify the electronic prop-

TABLE II. Calculated band gap values of $FASiI_3$ obtained using the GGA-PBE and TB-mBJ approximations.

Method	Band gap (eV)	Other works
GGA-PBE	0.48	0.66 [30], 1.46 [27]
TB-mBJ	0.59	–

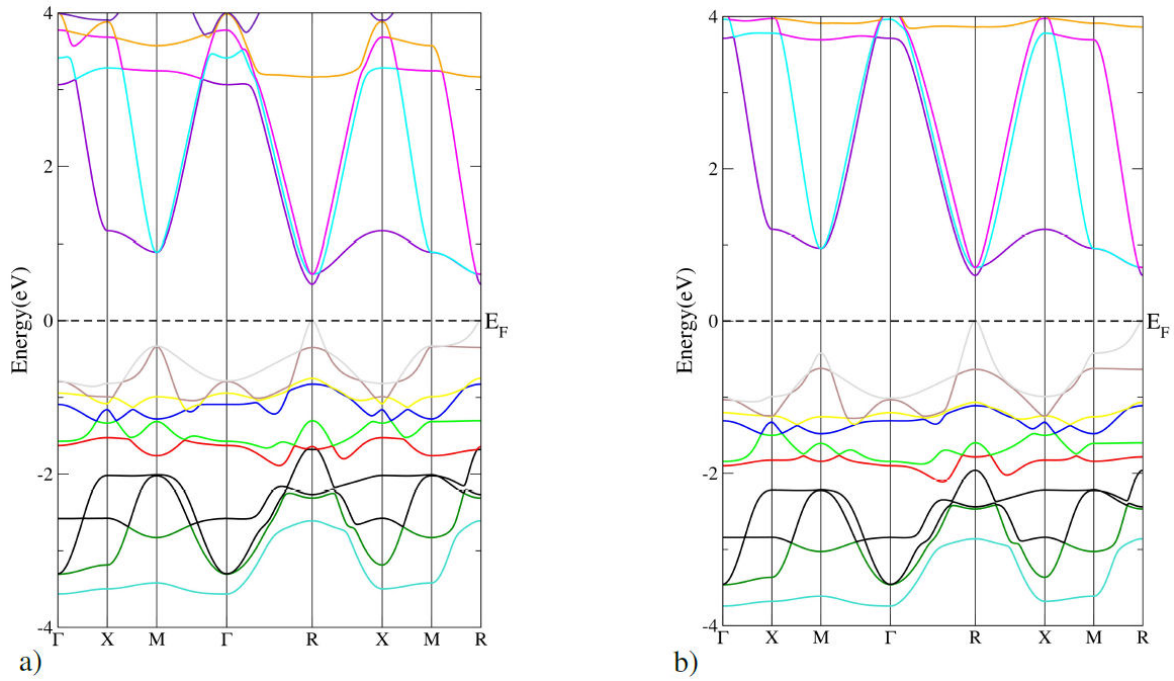

FIGURE 3. Band structure curve of $FASiI_3$ perovskite: a) GGA-PBE; b) TB-mBJ.

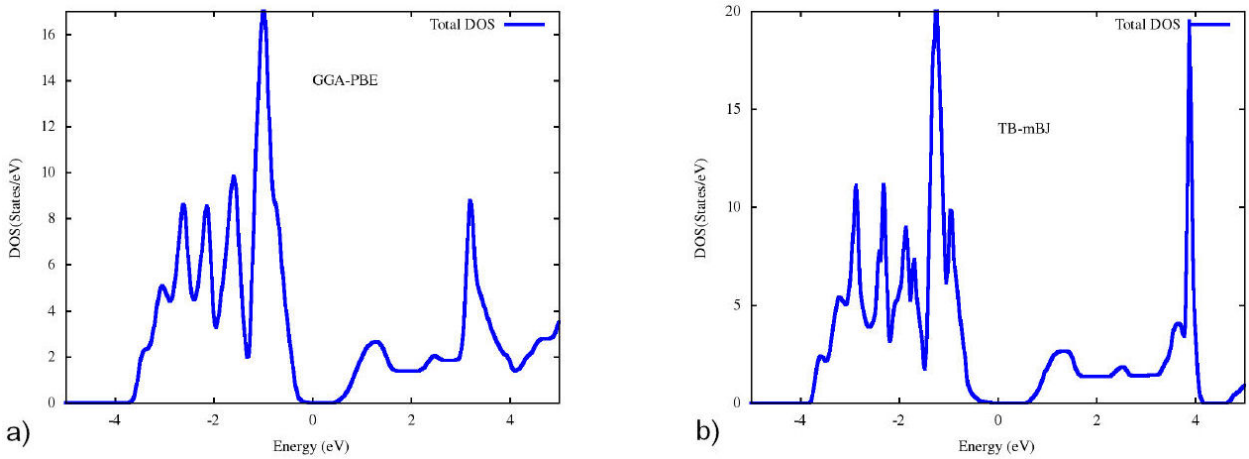

FIGURE 4. TDOS of $FASiI_3$ with a) GGA-PBE; b) TB-mBJ.

erties of this material and enhance its semiconductivity. Results demonstrate the functional choice is a strong factor that influences the accuracy with which the electronic states are represented and, in turn, provides predictions for the optoelectronic characteristics of the material.

3.3. Optical properties

3.3.1. Dielectric function

In this section, we calculated the real and imaginary parts, $\varepsilon_1(\omega)$ and $\varepsilon_2(\omega)$, respectively, of the dielectric constant, as well as the absorption coefficient, reflectivity, refractive index, extinction coefficient, and loss function using GGA-PBE and TB-mBJ. The optical parameters were examined in the UV-Vis-NIR spectrum over an energy range from 0 to 14 eV, to study the response of $FASiI_3$ to incident photons. The complex dielectric function is expressed as [41,42]:

$$\varepsilon(\omega) = \varepsilon_1(\omega) + i\,\varepsilon_2(\omega), \tag{4}$$

where $\varepsilon_1(\omega)$ is calculated with the Kramer-Kronig equation [43,44]

$$\varepsilon_1(\omega) = \frac{2}{\pi}\,\mathcal{P}\int_0^{\infty} \frac{\omega'\varepsilon_2(\omega')}{\omega'^2 - \omega^2}\,d\omega, \tag{5}$$

where, $\mathcal{P}$ is Cauchy's principal value of the integral.The $\mathrm{Re} - \varepsilon(\omega)$ component of the $\varepsilon(\omega)$ function determines the polarization of light and the dispersion of incident photons on the material, while the $\mathrm{Im} - \varepsilon(\omega)$ component represents

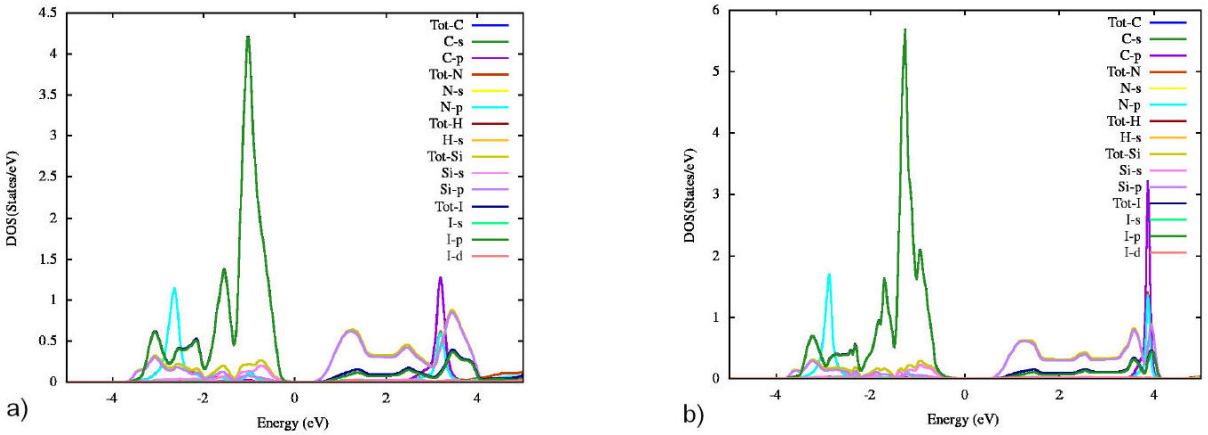

FIGURE 5. PDOS of $FASiI_3$ perovskite: a) GGA-PBE; b) TB-mBJ.

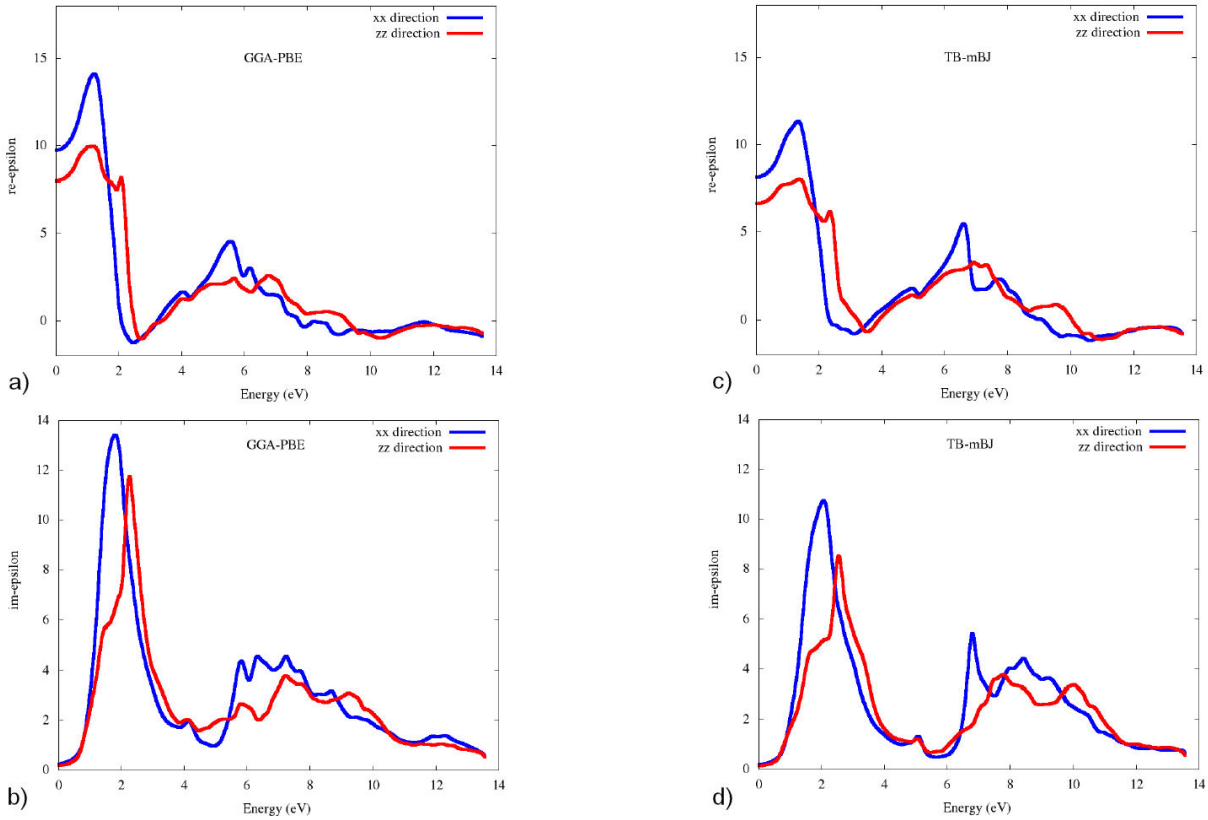

FIGURE 6. Real and imaginary parts of $FASiI_3$: a), b) GGA-PBE; c), d) TB-mBJ.

the material's light absorption properties. The equation below is used to provide this function:

$$\varepsilon_2(\omega) = \frac{e^2\hbar^2}{\pi m^2\omega^2}\sum_{v,c}|\langle\psi_c|\hat{\mathbf{e}}_j\cdot\mathbf{P}|\psi_v\rangle|^2 \times \delta(E_c - E_v - \hbar\omega). \quad (6)$$

Initially, the electron is in the valence band (VB) state denoted by ψ_v with the energy eigenvalue E_v. A photon with energy $\hbar\omega$ interacts with the electron providing it with enough kinetic energy to transition to a conduction band state (CB) ψ_c [45]. The probability during the transition of an electron from the VB state to the CB state is described by the elements of the momentum matrix:

$$\langle\psi_c|\hat{\mathbf{e}}_j\cdot\mathbf{P}|\psi_v\rangle. \quad (7)$$

where $\mathbf{P}$, m, and e represent the momentum operator, the mass, and the electronic charge of the electron, respectively.

The $\varepsilon_1(\omega)$ and $\varepsilon_2(\omega)$ spectra of $FASiI_3$ for both exchange-correlation approximations are plotted in Fig. 6.

TABLE III. Static dielectric constant $\varepsilon_1(0)$ of $FASiI_3$ calculated using the GGA-PBE and TB-mBJ approximations.

	GGA-PBE		TB-mBJ	
Direction	xx	zz	xx	zz
$\varepsilon_1(0)$	9.7	8.0	8.1	6.6

Considering the anisotropy of the material in the xx and zz axes, the results show differences between these two calculation methods, affecting both the real and imaginary parts.

$\varepsilon_1(\omega)$ spectra calculated with both approximations show similar behavior, with slightly different intensities in the xx direction. The results obtained using the two approximations for $\varepsilon_1(0)$ are summarized in Table III.

A sharp peak appears between 1 and 2 eV, and the contribution of the real part between 2 and 3 eV can be attributed to the characteristic interband transitions of excited electrons from the VB to the CB. After this decrease, an increase in $\varepsilon_1(\omega)$ is observed in the 3-6 eV range; this explains the gradual increase in the dielectric constant for these energies and its further decrease to around 12 eV. These changes indicate that a strong dielectric response occurs at low energies for the given $FASiI_3$ material, while it decreases at high energies due to the absence of absorption.

The imaginary part $\varepsilon_2(\omega)$ defines the absorption of light by the material and shows a different nature in both approximations. In GGA-PBE, across the xx direction, it shows a maximum peak at 2 eV, which describes the maximum absorption of light in this particular direction due to intense interband electronic transitions at this energy level. In the case of TB-mBJ, it occurs at the same position, 2 eV, but with reduced intensity compared to the one obtained using GGA-PBE. The fact that TB-mBJ reduces the intensity is expected because this method provides a more realistic view of energy levels and a band gap, which reduces the overestimation of absorption occurring in GGA-PBE.

3.3.2. *Absorption coefficient*

The material's capacity to generate electron-hole pairs is indicated by the absorption coefficient value. So, in order to employ these materials in optoelectronic applications, it seems required to examine the rate of light absorption specific to these materials [46]. Both approximations are used to investigate the absorption coefficient $\alpha(\omega)$. Being frequency-dependent, it can be calculated using the Im -$\varepsilon(\omega)$ component of the complex dielectric function. The subsequent equation describes the correlation between the absorption coefficient and the dielectric function [47]:

$$\alpha(\omega) = \frac{\omega}{c}\sqrt{2}\left[\sqrt{\varepsilon_1^2(\omega)+\varepsilon_2^2(\omega)} - \varepsilon_1(\omega)\right]^{\frac{1}{2}}. \qquad (8)$$

Figure 7 shows the behavior of the absorption-coefficient with photon energy for the two main directions of the material, with the two approximations. The absorption curves in both directions, show similar behavior, with significant differences in terms of peak intensity and structure. In the *NIR-visible-UV* range, as the incident light shifts from red to violet, the absorption coefficient increases linearly, reaching a maximum around 2 eV, with a value of $5 \times 10^5\,\mathrm{cm}^{-1}$.

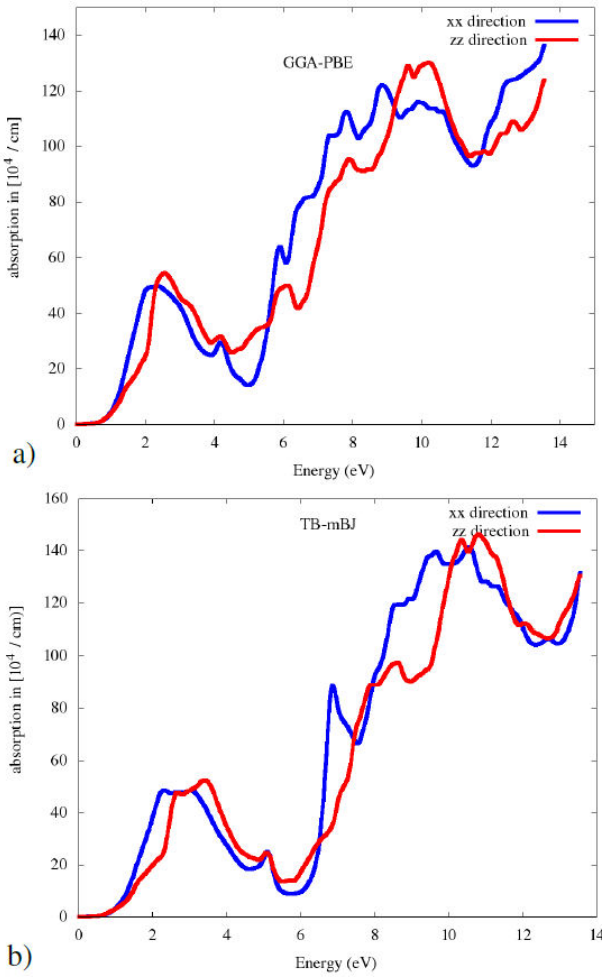

FIGURE 7. The absorption coefficient of $FASiI_3$ throughout the xx and zz direction with a) GGA-PBE , b) TB-mBJ.

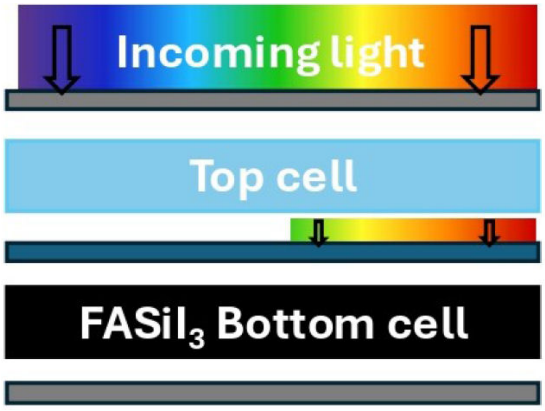

FIGURE 8. 2T tandem solar cell with $FASiI_3$ as the bottom absorber.

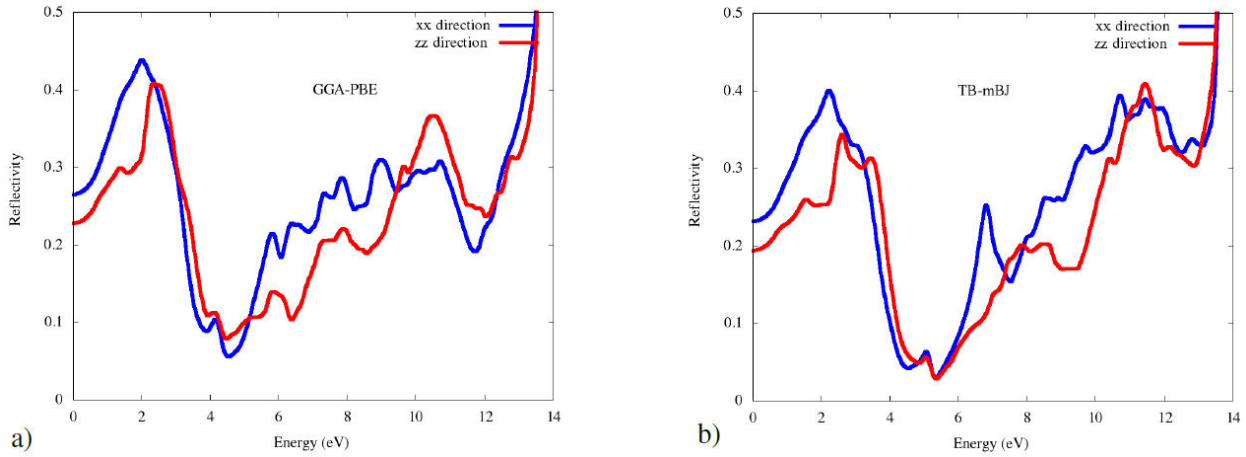

FIGURE 9. Reflectivity of $FASiI_3$ throughout the xx and zz direction with a) GGA-PBE, b) TB-mBJ.

Beyond this point, the absorption coefficient decreases in the *UV range*, reaching its minimum between 5 and 6 eV. Subsequently, it begins to rise rapidly, accompanied by fluctuations due to interband transitions, ultimately reaching a value on the order of 1.4×10^6 cm^{-1}. This behavior makes the material particularly well-suited for tandem solar cell applications as shown in Fig. 8.

3.3.3. *Reflectivity*

For solar absorbers in photovoltaic systems, the highest priority is achieving low reflectivity to ensure that nearly all incident solar radiation is absorbed and converted into usable energy [48]. This low reflectivity is intrinsically linked to the material's complex dielectric function, $\varepsilon(\omega)$, since at normal incidence the reflectivity can be expressed as [49]

$$R = \left| \frac{\sqrt{\varepsilon(\omega)} - 1}{\sqrt{\varepsilon(\omega)} + 1} \right|^2 . \tag{9}$$

In Fig. 9, the reflectivity curves reveal pronounced optical anisotropy, showing distinct differences between the xx and zz crystallographic directions. The GGA-PBE functional yields a smaller band gap, so its reflectivity onset and main peaks occur at lower energies compared to the TB-mBJ results, which shift the spectrum upward due to a larger predicted band gap consistent with the absorption curves.We also observe that, in both approximations, the reflectivity reaches a maximum for the xx direction around 2.1 and 2.6 eV, and for the zz direction around 2.3 and 3 eV, respectively. It then significantly decreases in the visible range and part of the UV, down to 4.5 and 5.3 eV, making $FASiI_3$ a promising candidate as a bottom absorber in tandem solar cells.

TABLE IV. Calculated static reflectivity $R(0)$ of $FASiI_3$ along the xx and xx directions using the GGA-PBE and TB-mBJ approaches.

	GGA-PBE		TB-mBJ	
Direction	xx	zz	xx	zz
$R(0)$	0.26	0.23	0.23	0.19

3.3.4. *Refractive index and Extinction coefficient*

The refractive index $n(\omega)$ and the extinction coefficient $\kappa(\omega)$ are the most important parameters because the complex refractive index [50] and $\varepsilon(\omega)$ are related by :

$$\varepsilon(\omega) = \tilde{n}^2, \tag{10}$$

with

$$\tilde{n} = n + i\kappa. \tag{11}$$

In HHP, a high $n(\omega)$ (typically between 2.0 and 2.5) promotes strong light confinement and effective absorption [51-53], while an optimized $\kappa(\omega)$ enhances the attenuation of incident light, thereby reducing parasitic losses. Tailoring these parameters through careful control of material composition and nanostructuring leads to selective absorber coatings with high solar absorptance, which in turn maximizes overall device efficiency [54].

Both curves 10a) and 10b), exhibit relatively high refractive index $n(\omega)$ values around low photon energies (below 2 eV), indicating strong dispersion just above the band gap, a common feature in semiconductors and perovskites where the refractive index peaks near the onset of electronic transitions. In the mid-energy range (2 eV; 6 eV), several pronounced peaks arise due to interband transitions from valence to higher conduction bands, with their precise positions and magnitudes shifting according to the chosen functional. Finally, in the high-energy (> 6 eV), $n(\omega)$ gradually decreases toward unity as photon energies exceed typical band-to-band transition energies, although residual peaks can occur from deeper core-level or higher-energy transitions. Table V summarizes the static $n(0)$ along both directions.

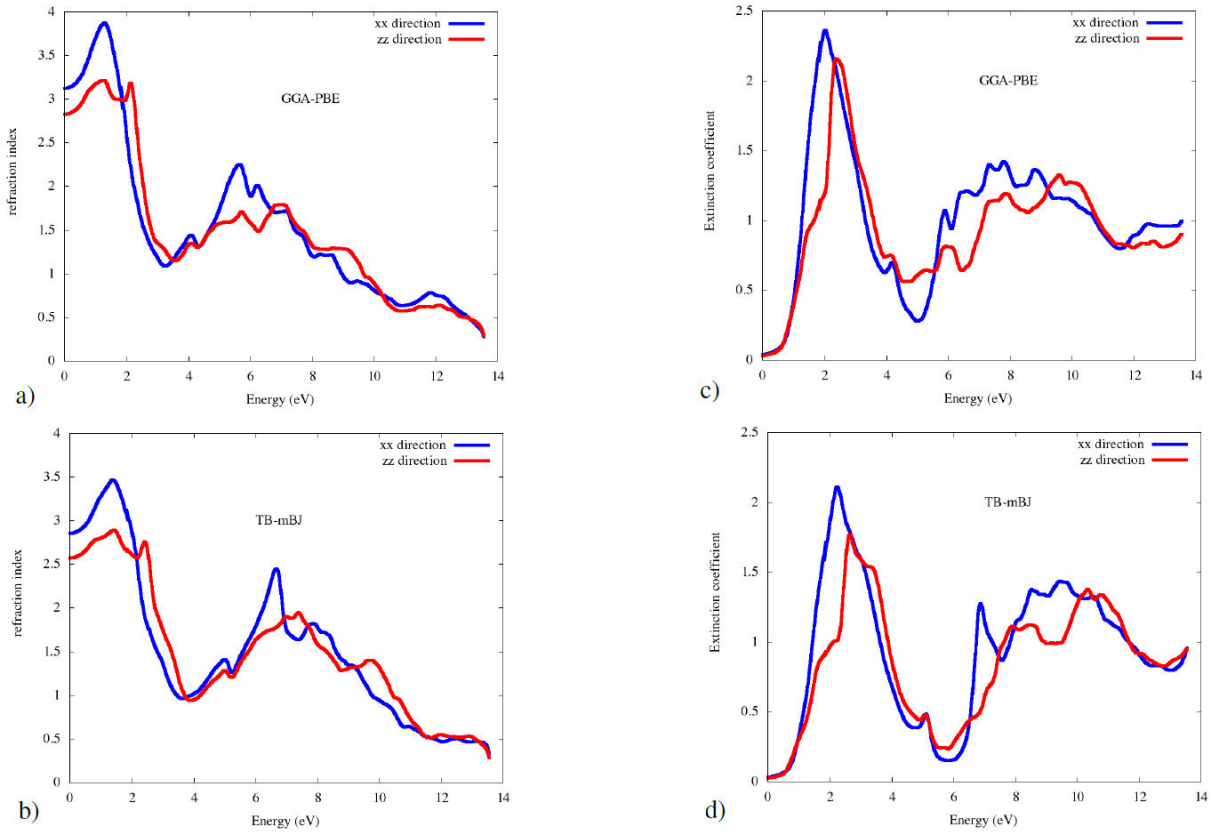

FIGURE 10. $n(\omega)$ and $\kappa(\omega)$ of $FASiI_3$ throughout the xx and zz direction with a) GGA-PBE, b) TB-mBJ.

TABLE V. Calculated static refractive index $n(0)$ of $FASiI_3$ along the xx and zz directions using the GGA-PBE and TB-mBJ approaches.

	GGA-PBE		TB-mBJ	
Direction	xx	zz	xx	zz
$n(0)$	0.26	0.23	0.23	0.19

In Figs. 10c) and 10d) the energy range from 0.0 to approximately 2.0 eV, $\kappa(\omega)$ remains close to zero, indicating that electromagnetic waves can pass through the material without significant absorption. This confirms the transparency of $FASiI_3$ in this spectral region, aligning with the band gap energy of the material. The first major peak appears in the visible-near UV region, located at 2.0 eV for both xx and zz polarization modes. This peak corresponds to direct interband electronic transitions from the valence to the conduction band and marks the onset of significant optical absorption. Compared to GGA-PBE, the TB-mBJ calculation shifts this peak slightly to higher energy, reflecting the improved band gap estimation of this functional. A second prominent peak is observed in the deep UV region, around $6-8$ eV, with slightly different positions for xx and zz polarizations. This anisotropy suggests a direction-dependent interaction of the material with electromagnetic waves. At even higher energies, multiple oscillations in $\kappa(\omega)$ indicate a complex interplay of electronic transitions involving deeper states in the valence band. Overall, the TB-mBJ approach provides a more accurate representation of the optical absorption features, in agreement with its improved electronic structure description. These results align well with the behavior observed in the absorption coefficient spectrum, confirming the material's strong optical anisotropy and its potential applicability in optoelectronic devices.

3.3.5. *Loss function*

The loss function, denoted as $L(\omega)$, is a critical parameter that describes the energy dissipation of electromagnetic waves within the absorber material. It is mathematically defined as the negative imaginary part of the inverse dielectric function [55]:

$$L(\omega) = \mathrm{Im}\left[-\frac{1}{\varepsilon(\omega)}\right]. \tag{12}$$

This function provides insight into the material's response to external electromagnetic fields, particularly in processes like electron energy loss spectroscopy (EELS), where it represents the probability of energy loss by fast electrons traversing the material [56].

The loss function is instrumental in identifying various excitations within the material, such as plasmons, interband transitions, and other collective oscillations. Peaks in $L(\omega)$

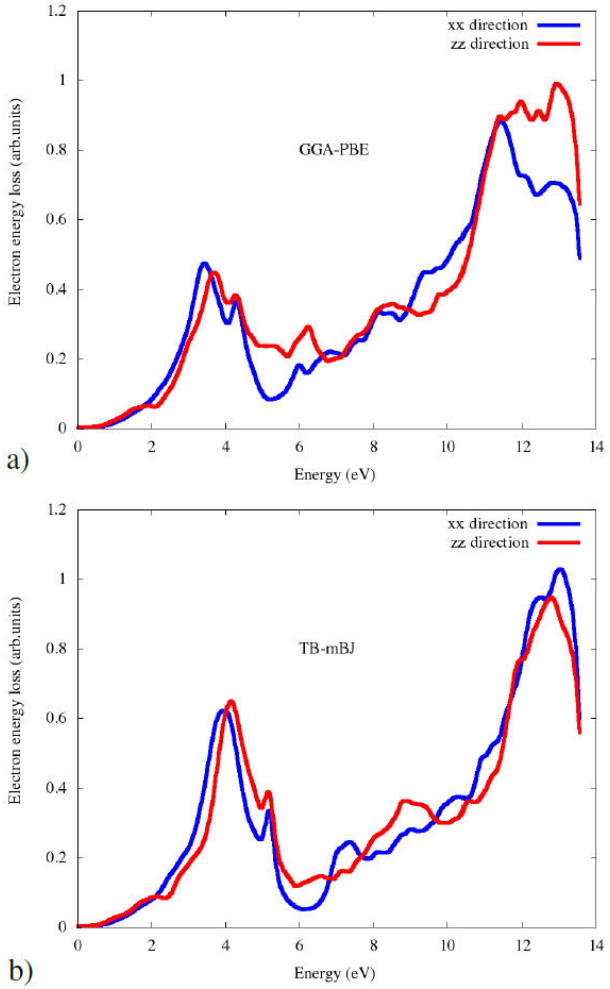

FIGURE 11. Loss function $L(\omega)$ of $FASiI_3$ throughout the xx and zz direction with a) GGA-PBE, b) TB-mBJ.

correspond to resonant frequencies where energy dissipation is significant, indicating strong interactions between the electromagnetic field and the material's electronic structure [57].

Understanding and analyzing the loss function aids in the design and optimization of materials for applications like plasmonics, photonic devices, and other technologies where control over light-matter interactions is essential [58].

Figure 11 shows the electronic energy-loss function, calculated for two crystallographic orientations xx and zz. It is immediately apparent that the TB-mBJ results which are more effective at accurately predicting the band gap exhibit characteristic peaks shifted to higher energies relative to the GGA-PBE calculations. This shift can be attributed to a more precise treatment of the band structure. In both cases, the main peak observed between 10 and 14 eV typically corresponds to the bulk plasmon resonance, which occurs when $\varepsilon_1(\omega)$, crosses zero. Moreover, secondary peaks in the 5–10 eV range can be associated with interband transitions or with more localized valence plasmons. A comparison between the xx and zz directions reveals a moderate anisotropy; slight differences in the peak positions and intensities suggest that the electronic dispersion differs along the out-of-plane zz axis relative to the in-plane xx direction. Overall, these results underscore both the impact of the chosen exchange-correlation potential (TB-mBJ versus GGA-PBE) on the energy and amplitude of the peaks and the intrinsic anisotropic optical response of the material as reflected in the divergence between the xx and zz curves.

4. Conclusion

This study presents a comparative analysis of the structural and optoelectronic properties of $FASiI_3$ using two distinct computational methodologies: the GGA-PBE functional and the TB-mBJ exchange-correlation potential. Our findings demonstrate that $FASiI_3$ crystallizes in a cubic lattice (space group Pm3m) with an equilibrium lattice constant of $a = 6.29$ Å. Electronic structure calculations reveal that the TB-mBJ approach provides a more accurate description of the material's semiconducting behavior, as evidenced by its direct bandgap.

Optical property investigations highlight pronounced anisotropy in reflectivity and absorption spectra, with distinct directional dependencies observed along the (xx) and (zz) crystallographic axes. Notably, the absorption coefficient exceeds 10^5 cm^{-1} within the NIR solar spectrum range, positioning $FASiI_3$ as a highly efficient light-harvesting material. These results, coupled with its favorable charge transport characteristics, strongly advocate for $FASiI_3$'s inclusion in next-generation optoelectronic devices, particularly in tandem solar cell systems designed for solar energy conversion.

1. F. Elfatouaki *et al.*, Enhanced stability and optoelectronic properties of double perovskite Cs2AgSbI6 by Br doping for solar cells, *Mater. Today Sustain.* **24** (2023) 100572, https://doi.org/10.1016/j.mtsust.2023.100572

2. A. Jana *et al.*, Perovskite: Scintillators, direct detectors, and X-ray imagers, *Mater. Today* **55** (2022) 110, https://doi.org/10.1016/j.mattod.2022.04.009

3. G. Getachew *et al.*, Metal halide perovskite nanocrystals for biomedical engineering: Recent advances, challenges, and future perspectives, *Coord. Chem. Rev.* **482** (2023) 215073, https://doi.org/10.1016/j.ccr.2023.215073

4. H. Lu *et al.*, Vapor-assisted deposition of highly efficient, stable black-phase FAPbI3 perovskite solar cells, *Science* **370** (2020) eabb8985, https://doi.org/10.1126/science.abb8985

5. A. A. Zhumekenov *et al.*, Formamidinium lead halide perovskite crystals with unprecedented long carrier dynamics and diffusion length, *ACS Energy Letters* **1** (2016) 32, https:

//doi.org/10.1021/acsenergylett.6b00002

6. Y. N. Kavil *et al.*, Electronic waste and environmental diplomacy: How GCC E-waste management interfaces with the Stockholm Convention, *Journal of Hazardous Materials Advances* (2025) 100610, https://doi.org/10.1016/j.hazadv.2025.100610
7. A. Jana *et al.*, Stabilization of halide perovskites with silicon compounds for optoelectronic, catalytic, and bioimaging applications, *InfoMat* **6** (2024) e12559, https://doi.org/10.1002/inf2.12559
8. S. Pachori *et al.*, Mechanically stable with highly absorptive formamidinium lead halide perovskites [(HC (NH2) 2PbX3; X= Br, Cl]: Recent advances and perspectives, International *Journal of Quantum Chemistry* **121** (2021) e26671, https://doi.org/10.1002/qua.26671
9. D. B. Mitzi *et al.*, Conducting tin halides with a layered organic-based perovskite structure, *Nature* **369** (1994) 467, https://doi.org/10.1038/369467a0
10. Q. Fu *et al.*, Recent progress on the long-term stability of perovskite solar cells, *Advanced science* **5** (2018) 1700387, https://doi.org/10.1002/advs.201700387
11. H. El-Ghtami, A. Laref, and S. Laref, Electronic and optical behaviors of methylammonium and formamidinium lead trihalide perovskite materials, *Journal of Materials Science: Materials in Electronics* **30** (2019) 711, https://doi.org/10.1007/s10854-018-0340-2
12. S. Pachori *et al.*, First-principles calculations for fundamental and spectroscopic screening of hybrid perovskite (HC (NH2) 2PbI3) formamidinium lead iodide, *Materials Chemistry and Physics* **287** (2022) 126149, https://doi.org/10.1016/j.matchemphys.2022.126149
13. F. Mahajabin *et al.*, Role of compressive and tensile strains and spin-orbit coupling on structure and behaviors of cubic FAPbI3 perovskites: a first-principles prediction, *Materials Chemistry and Physics* **313** (2024) 128763, https://doi.org/10.1016/j.matchemphys.2023.128763
14. F. Elfatouaki *et al.*, Enhancing Perovskite Solar Cells Performance Through Investigation of Ruddlesden-Popper (2D) Cs2GeI2Br2 and (3D) CsGeI2Br Absorbers, *The Journal of Physical Chemistry C* **128** (2024) 19962, https://doi.org/10.1021/acs.jpcc.4c04167
15. P. Kanhere *et al.*, Substitution induced band structure shape tuning in hybrid perovskites (CH 3 NH 3 Pb 1- x Sn x I 3) for efficient solar cell applications, *RSC advances* **5** (2015) 107497, https://doi.org/10.1039/C5RA19778C
16. S. Lv *et al.*, One-step, solution-processed formamidinium lead trihalide (FAPbI (3- x) Cl x) for mesoscopic perovskite-polymer solar cells, *Physical Chemistry Chemical* Physics **16** (2014) 19206, https://doi.org/10.1039/C4CP02113D
17. J. Hakami, Enhancing the efficiency of methylammonium silicon iodide-based perovskite solar cells: Optimization of charge transport layers and device parameters, *Results in Engineering* **25** (2025) 104401, https://doi.org/10.1016/j.rineng.2025.104401
18. Z. Chailoo, H. Noshad, and A. Doroudi, Ab-initio investigation of the structural, electronic and optical properties of CsPbBr3 perovskite under pressure using the DFT-1/2 method, *Physica B: Condensed Matter* **686** (2024) 415999, https://doi.org/10.1016/j.physb.2024.415999
19. M. Tahir *et al.*, First principle study of structural, electronic, elastic and optical properties of tixf 3 (x= ag and pd) employing accurate tb-mbj approach., *Fluoride* **56** (2023).
20. R. Takassa *et al.*, Structural and electronic properties of Ndoping ultra-small diameter (3,3) armchair SWCNT by using PBE and TB-mBJ potentials, *Applied Surface Science* **563** (2021) 150283, https://doi.org/10.1016/j.apsusc.2021.150283
21. I. Salym *et al.*, Optoelectronic enhancement and exciton control in Si-doped KGeF3 perovskites, *Physica B: Condensed Matter* **734** (2026) 418619, https://doi.org/10.1016/j.physb.2026.418619
22. S. Blügel and G. Bihlmayer, Full-potential linearized augmented planewave method, *Computational nanoscience: do it yourself* **31** (2006) 85.
23. O. Farkad *et al.*, Improving thermoelectric properties of Bernal bilayer graphene by strontium intercalation: A DFT study, *Diamond and Related Materials* **141** (2024) 110590, https://doi.org/10.1016/j.diamond.2023.110590
24. F. Elfatouaki *et al.*, Electronic and optical properties of CsGeX2M (X, M= Br, Cl, I) perovskites for solar cell applications: First-principles study using PBE and TB-mBJ potentials, *Materials Science in Semiconductor Processing* **143** (2022) 106488, https://doi.org/10.1016/j.mssp.2022.106488
25. K. Schwarz and P. Blaha, Solid state calculations using WIEN2k, *Computational Materials Science* **28** (2003) 259, https://doi.org/10.1016/S0927-0256(03)00112-5
26. S. Hassine *et al.*, Electronic and optical properties of bulk Zn2VN3 ternary nitride: First-principles investigation, *Materials Science in Semiconductor Processing* **166** (2023) 107725, https://doi.org/10.1016/j.mssp.2023.107725
27. Y. El Arfaoui, M. Khenfouch, and N. Habiballah, New narrow band gap of silicon-based perovskite FASiI3 for photovoltaic applications: first principle investigations of the structural, electronic and optical properties, *The European Physical Journal B* **97** (2024) 19, https://doi.org/10.1140/epjb/s10051-024-00655-x
28. A. A. Pasha *et al.*, Computational study of the physical characteristics of Si-based oxide perovskites for energy generation using DFT, *Materials Advances* **4** (2023) 6645, https://doi.org/10.1039/D3MA00537B
29. F. Murnaghan, On the theory of the tension of an elastic cylinder, *Proceedings of the National Academy of Sciences* **30** (1944) 382, https://doi.org/10.1073/pnas.30.12.382
30. F. Valadares *et al.*, Electronic structure panorama of halide perovskites: approximated DFT-1/2 quasiparticle and relativistic corrections, *The Journal of Physical Chemistry C* **124** (2020) 18390, https://doi.org/10.1021/acs.jpcc.0c03672

31. K. Assiouan *et al.*, Theoretical investigation of Rb2AuBiX6 (X= Br, cl, F) double perovskite for thermoelectric and optoelectronic applications, *Journal of Physics and Chemistry of Solids* **188** (2024) 111890, https://doi.org/10.1016/j.jpcs.2024.111890

32. P. Gao, M. Grätzel, and M. K. Nazeeruddin, Organohalide lead perovskites for photovoltaic applications, *Energy & Environmental Science* **7** (2014) 2448, https://doi.org/10.1039/C4EE00942H

33. J. Huang *et al.*, Understanding the physical properties of hybrid perovskites for photovoltaic applications, *Nature Reviews Materials* **2** (2017) 1, https://doi.org/10.1038/natrevmats.2017.42

34. H.-Y. Ye *et al.*, Metal-free three-dimensional perovskite ferroelectrics, *Science* **361** (2018) 151, https://doi.org/10.1126/science.aas9330

35. Z. Yang, A. Rajagopal, and A. K.-Y. Jen, Ideal bandgap organic-inorganic hybrid perovskite solar cells, *Advanced Materials* **29** (2017) 1704418, https://doi.org/10.1002/adma.201704418

36. F. Meinardi *et al.*, Highly efficient luminescent solar concentrators based on earth-abundant indirect-bandgap silicon quantum dots, *Nature Photonics* **11** (2017) 177, https://doi.org/10.1038/nphoton.2017.5

37. Z. Chen *et al.*, Thin single crystal perovskite solar cells to harvest below-bandgap light absorption, *Nature communications* **8** (2017) 1890, https://doi.org/10.1038/s41467-017-02039-5

38. C. Kittel and P. McEuen, Introduction to solid state physics (John Wiley & Sons, 2018), pp. 465-486.

39. P. Hohenberg and W. Kohn, Inhomogeneous electron gas, *Physical review* **136** (1964) B864, https://doi.org/10.1103/PhysRev.136.B864

40. R. Takassa *et al.*, Investigation of the electronic and thermoelectric properties of nitrogen chains doping SWCNT: ab initio study, *The European Physical Journal Applied Physics* **98** (2023) 32, https://doi.org/10.1051/epjap/2023230013

41. H. Ehrenreich, H. Philipp, and B. Segall, Optical properties of aluminum, *Physical Review* **132** (1963) 1918, https://doi.org/10.1103/PhysRev.132.1918

42. M. Fox, Optical properties of solids, vol. **3** (Oxford university press, 2010).

43. F. Wooten, Optical properties of solids (Citeseer, 1972).

44. P. C. Martin, Sum rules, Kramers-Kronig relations, and transport coefficients in charged systems, *Physical Review* **161** (1967) 143, https://doi.org/10.1103/PhysRev.161.143

45. F. Elfatouaki *et al.*, Optoelectronic and thermoelectric properties of double halide perovskite Cs2AgBiI6 for renewable energy devices, *Solar Energy* **260** (2023) 1, https://doi.org/10.1016/j.solener.2023.05.032

46. J. Hu *et al.*, All-dielectric metasurface circular dichroism waveplate, *Scientific Reports* **7** (2017) 41893, https://doi.org/10.1038/srep41893

47. K. Rajkanan, R. Singh, and J. Shewchun, Absorption coefficient of silicon for solar cell calculations, *Solid-State Electronics* **22** (1979) 793, https://doi.org/10.1016/0038-1101(79)90128-X

48. H. Zhang *et al.*, Efficient solar energy absorber based on titanium nitride metamaterial, *Plasmonics* **18** (2023) 2187, https://doi.org/10.1007/s11468-023-01932-8

49. Y. Zhang *et al.*, Photonics and optoelectronics using nanostructured hybrid perovskite media and their optical cavities, *Physics Reports* **795** (2019) 1, https://doi.org/10.1016/j.physrep.2019.01.005

50. H. Hakim *et al.*, Study the optical properties of Polyvinylpyrrolidone (PVP) doped with KBr, *European Scientific Journal* **3** (2013) 132.

51. A. S. Berestennikov *et al.*, Active meta-optics and nanophotonics with halide perovskites, *Applied Physics Reviews* **6** (2019), https://doi.org/10.1063/1.5107449

52. H. Jing *et al.*, Hybrid organic-inorganic perovskite metamaterial for light trapping and photon-to-electron conversion, *Nanophotonics* **9** (2020) 3323, https://doi.org/10.1515/nanoph-2020-0071

53. J. K. Singh, S. K. Mandal, and G. Banerjee, Refractive index of different perovskite materials, *Journal of Materials Research* **36** (2021) 1773, https://doi.org/10.1557/s43578-021-00257-8

54. T. Tesfamichael and E. Wäckelgard, Angular solar absorptance of absorbers used in solar thermal collectors, *Applied optics* **38** (1999) 4189, https://doi.org/10.1364/AO.38.004189

55. H. Philipp and H. Ehrenreich, Optical properties of semiconductors, *Physical Review* **129** (1963) 1550, https://doi.org/10.1103/PhysRev.129.1550

56. F. Hofer *et al.*, Fundamentals of electron energy-loss spectroscopy, In IOP Conference Series: Materials Science and Engineering, vol. **109** (IOP Publishing, 2016) p. 012007.

57. E. Fourkal, M. Lachaine, and B. Fallone, Signal formation in amorphous-Se-based x-ray detectors, *Physical Review B* **63** (2001) 195204, https://doi.org/10.1103/PhysRevB.63.195204

58. V. Giannini *et al.*, Plasmonic nanoantennas: fundamentals and their use in controlling the radiative properties of nanoemitters, *Chemical reviews* **111** (2011) 3888, https://doi.org/10.1021/cr1002672

59. R. K. Singh *et al.*, Investigation of optical and dielectric properties of CsPbI3 inorganic lead iodide perovskite thin film, *Journal of the Taiwan Institute of Chemical Engineers* **96** (2019) 538, https://doi.org/10.1016/j.jtice.2018.11.001